

Journal of Materials Chemistry C

Materials for optical, magnetic and electronic devices

Accepted Manuscript

This article can be cited before page numbers have been issued, to do this please use: S. S. Dixit, T. Desai, O. Kapur, B. Ding, R. Huang and C. Gurnani, *J. Mater. Chem. C*, 2026, DOI: 10.1039/D6TC00598E.



This is an Accepted Manuscript, which has been through the Royal Society of Chemistry peer review process and has been accepted for publication.

Accepted Manuscripts are published online shortly after acceptance, before technical editing, formatting and proof reading. Using this free service, authors can make their results available to the community, in citable form, before we publish the edited article. We will replace this Accepted Manuscript with the edited and formatted Advance Article as soon as it is available.

You can find more information about Accepted Manuscripts in the [Information for Authors](#).

Please note that technical editing may introduce minor changes to the text and/or graphics, which may alter content. The journal's standard [Terms & Conditions](#) and the [Ethical guidelines](#) still apply. In no event shall the Royal Society of Chemistry be held responsible for any errors or omissions in this Accepted Manuscript or any consequences arising from the use of any information it contains.

Molecular Precursor-Directed Growth of Nanostructured SnS_2 for Memristive and Neuromorphic Electronics

Suprabha S. Dixit^a, Trishala R. Desai^a, Omesh Kapur^b, Bohao Ding^b, Ruomeng Huang^{b},
Chitra Gurnani^{a*}*

^aDepartment of Chemistry, Ecole Centrale School of Engineering, Mahindra University,
Hyderabad-500043, India

^bSchool of Electronics and Computer Science, University of Southampton, Southampton, UK

Corresponding Author Email:

^{a*}chitra.gurnani@mahindrauniversity.edu.in

^{b*}r.huang@soton.ac.uk



Abstract

View Article Online
DOI: 10.1039/D6TC00598E

Low-dimensional layered metal chalcogenides have recently garnered significant attention for advanced electronic and optoelectronic applications, particularly memristive and synaptic devices; however, achieving purity and scalable fabrication remains a key challenge. We demonstrate a facile and scalable in-situ solvothermal approach enabling low-temperature deposition of SnS₂ thin films, employing the single-source precursor (SSP) [Cl₂Sn(S₂P(OⁱC₃H₇)₂)₂]. The distorted octahedral complex [Cl₂Sn(S₂P(OⁱC₃H₇)₂)₂], derived from SnCl₄, serves as an efficient SSP for solvothermal growth of SnS₂ on ITO. The films exhibit phase-pure hexagonal crystallinity with well-defined composition and morphology, and an optical bandgap of 2.06 eV. Leveraging this synthesis route, Ag/SnS₂/ITO memristive device was fabricated, exhibiting electroforming-free bipolar resistive switching at ±0.6 V. The device demonstrated stable endurance over more than 10² cycles with an ON/OFF ratio of ~10. Additionally, the device further exhibits analogue conductance modulation and synaptic plasticity, enabling emulation of biological learning behaviour when implemented in a hardware-aware artificial neural network. The experimentally derived weight update dynamics achieved 92% classification accuracy on the MNIST dataset. Collectively, these findings establish SSP-derived SnS₂ thin films as a viable material platform for emerging memory and neuromorphic electronics.



1. Introduction

Tin disulphide (SnS_2), a layered post-transition metal chalcogenide, has emerged as a versatile material for energy, memory, and photonic applications due to its appropriate band gap (~ 2.2 eV)¹ high charge carrier mobility ($\sim 230 \text{ cm}^2 \text{ V}^{-1} \text{ s}^{-1}$),² robust chemical and thermal stability. As a group-IVA semiconducting metal chalcogenide composed of earth-abundant and environmentally benign elements, tin sulphide represents a low-cost materials platform. Structurally, SnS_2 adopts a CdI_2 -type layered structure analogous to that of conventional transition metal dichalcogenides (TMDCs) (e.g., MoS_2 and WS_2), resulting in weak interlayer van der Waals interactions and pronounced two-dimensional characteristics^{3,4}. In addition, SnS_2 exhibits rich structural polymorphism, with more than seventy reported polytypes, including the 4H and 18R phases.⁵ This hexagonal layered structure, bound by weak van der Waals interactions,⁶ enables scalable fabrication of high-quality thin films suitable for device integration.⁷

Despite these advantages, conventional routes for the synthesis of SnS_2 thin films predominantly rely on dual-source precursor (DSP) systems, multistep processing, or hazardous sulphur reagents such as H_2S , which collectively limit process simplicity, safety, and scalability. In most reported studies, SnS_2 films are deposited from separate tin and sulphur sources (e.g., SnCl_4 and H_2S), necessitating stringent control over precursor delivery to achieve stoichiometric composition while introducing significant handling and environmental concerns. To mitigate these challenges, a range of single-source precursors (SSPs) has been investigated, including thiolates and dithiolates such as $\text{Sn}(\text{SCH}_2\text{CF}_3)_4$, $\text{Sn}(\text{SPh})_4$, $\text{Sn}(\text{SCy})_4$,^{8,9} and $\text{Sn}(\text{SCH}_2\text{CH}_2\text{S})_2$,¹⁰ dithiocarbamates and unsymmetrical dithiocarbamates such as $\text{Sn}(\text{S}_2\text{CNEt}_2)_4$,¹¹ and $\{\text{R}_n\text{Sn}[\text{S}_2\text{CN}(\text{C}_4\text{H}_9)\text{CH}_3]_{4-n}\}$, where $\text{R} = \text{Me}, \text{Bu}, \text{or Ph}$ and $n = 1, 2, \text{ or } 3$.¹² Nevertheless, a lot of these SSP systems still need external H_2S as an additional source of sulphur, post-deposition treatments, or binder-assisted processing, thereby increasing synthetic



complexity and limiting scalability. In parallel, deposition of phase-pure SnS₂ thin films has largely relied on techniques that are costly, complex, and difficult to scale for large-area fabrication.¹³ Common approaches include mechanical exfoliation,³ chemical vapour deposition (CVD)^{14,15} and physical epitaxy¹⁶. Although CVD and epitaxial growth can yield uniform films, their elevated processing temperatures often exceed the thermal budgets of technologically relevant substrates. Mechanical exfoliation, while capable of producing high-quality flakes, suffers from low yield and poor scalability.¹⁷ Collectively, these limitations highlight the need for a one-pot, non-toxic, low-temperature, and scalable strategy for the controlled growth of pure-phase nanostructured SnS₂ thin films.

SSP strategies offer a compelling solution by integrating all requisite elements within a single molecular framework.¹⁸ Such molecular-level stoichiometric preorganization enables precise compositional control while minimizing pre-reactions and sulphur deficiencies commonly encountered in DSP systems.¹⁹ Moreover, rational modification of precursor structure provides a direct handle over decomposition pathways, phase selectivity, nucleation behavior, and film morphology, rendering SSP-based approaches particularly attractive for scalable thin-film fabrication. Herein, we focus on dithiophosphate (DTP) complexes as effective SSPs owing to their versatile coordination chemistry, preformed metal-sulphur bonds, and favorable thermal decomposition characteristics.²⁰ These attributes enable the formation of low-dimensional metal sulphides under relatively mild processing conditions while maintaining long shelf life and synthetic simplicity. Importantly, the tunability of the dithiophosphate framework further provides a molecular-level handle over precursor stability, volatility, and decomposition pathways, making this class of compounds particularly attractive for the scalable growth of phase-controlled tin sulphide thin films.²¹ When combined with solution-based deposition strategies, such precursors offer a practical and scalable route for thin-film growth enables low-temperature and substrate-compatible deposition. This approach also provides control over



phase purity, crystallinity, and film morphology, parameters that directly influence material properties. To date, no DTP-based molecular precursor has been reported for the direct low-temperature growth of phase-pure SnS₂ thin films.

The ability to achieve stoichiometric, binder-free, high-purity SnS₂ nanostructured thin films at low temperature through SSP-based routes provides a well-defined platform for electronic device applications. As artificial intelligence (AI) continues to advance, neuromorphic technologies that emulate biological neural networks are increasingly recognized as promising alternatives to conventional von Neumann architectures.^{22,23} Within this landscape, SnS₂ has received comparatively less attention than other 2D materials^{24,25} and/or transition metal dichalcogenides (TMDs)²⁶, such as MoS₂ and WS₂. Nevertheless, recent studies have begun to highlight its potential for neuromorphic applications.²⁷ In this context, liquid-phase-synthesised SnS₂ quantum dot memristors have demonstrated intriguing resistive switching characteristics.²⁸ SnS₂-reduced graphene oxide (rGO) composites have been explored as electrochemical artificial synapses,²⁹ while SnO_x/SnS₂ heterostructures have exhibited enhanced switching performance with relevance to neuromorphic technologies.³⁰ Very recently, spin-coated SnS₂ doped with Ca²⁺ ions has been reported for memristive behavior and synaptic emulation.³¹ Collectively, these studies underscore the emerging potential of SnS₂ as an active material for next-generation neuromorphic architectures aimed at replicating the adaptive and learning functionalities of biological neural networks.

Herein, we report the synthesis and application of a new SSP, [Cl₂Sn(S₂P(O⁻C₃H₇)₂)₂], designed for low-temperature, one-step in-situ solvothermal deposition of stoichiometric, crystalline SnS₂ thin films. This precursor enables direct growth of binder-free hexagonal SnS₂ on ITO/glass substrates under mild solvothermal conditions, and post-treatment. The resulting films exhibit well-defined nanostructured morphology and phase purity, validated through compositional and structural characterization. To demonstrate functional relevance, the



solution-processed SnS₂ films were directly integrated into two-terminal resistive switching memory (RSM) devices. These devices demonstrated bipolar switching without forming or compliance, stable ON/OFF ratios and good endurance. Notably, the proposed pristine SnS₂-based memristors showed analog switching characteristics and synaptic behaviour, enabling emulation of biological plasticity and achieving 92% classification accuracy on the MNIST handwritten digit dataset in a hardware-aware artificial neural network (ANN) simulation.

2. Materials and Methods

2.1 Reagents and Materials

Tin tetrachloride (SnCl₄, 98%) and phosphorus pentasulphide (P₂S₅, 99%) were used as received from Alfa Aesar and Sigma-Aldrich, respectively. Toluene (C₇H₈, 99.5%), isopropanol (C₃H₈O, 99%), *n*-hexane (C₆H₁₄, 99%), and dichloromethane (DCM, CH₂Cl₂, 99.5%) were procured from S.D. Fine-Chem Limited, SRL, and FINAR, respectively. Every chemical was of analytical grade. Toluene and isopropanol were distilled before use. All experimental procedures were carried out in an inert atmosphere using vacuum and Schlenk-line techniques, with strict precautions to prevent exposure to moisture during handling. Global Nanotech provided glass substrates coated with indium tin oxide (ITO).

2.2 Synthesis of SSP and Characterization

[Et₃NH][[(OⁱC₃H₇)₂S₂P]]: The compound was prepared according to a previously described protocol for the propanol-based ligand.³² P₂S₅ (2.5 g, 1.12 mM) was gradually added to distilled toluene (20 mL) under stirring, after which freshly distilled isopropanol (3.36 mL, 4.48 mM) was added. The mixture was heated at 80–90 °C until complete dissolution of P₂S₅, then cooled to ambient temperature. Triethylamine (Et₃N, 3.2 mL, 2.24 mM) was added dropwise under stirring, followed by the addition of *n*-hexane to induce precipitation. After filtration, the resulting white precipitate was dried under reduced pressure to remove residual solvents. Yield:



(6.5 g, 88.3%); anal: M.W. of $C_{12}H_{30}O_2PS_2N$: 315.2; 1H NMR ($CDCl_3$, 298 K, δ ppm): 1.34 (t, [6H], -CH₃ of isopropanol), 1.42 (t, [9H], -CH₃ of Et₃N), 1.7 (m, [4H], -CH₂CH₃ of isopropanol), 3.3 (m, [4H], -CH₂ of isopropanol), 4.8 (m, [6H], CH₂ of Et₃N); $^{31}P\{^1H\}$ ($CDCl_3$, 298 K, δ ppm): 107.48 (s); IR (KBr) (cm^{-1}): 1166(s), ν [(P) O-C]; 863(s), ν [P-O-(C)]; 660(s), ν (P=S) and 553(s), ν (P-S).

$Cl_2Sn[S_2P(O^iC_3H_7)]_2$: A suspension of $\{[Et_3NH][O^iC_3H_7)_2S_2P]\}_2$ (2.025 g, 2.7 M) in toluene (20 mL) was prepared in an inert nitrogen atmosphere. Tin tetrachloride ($SnCl_4$, 0.377 mL, 0.9M) was dropwise added to the suspension using a syringe, maintaining a 1:2 molar ratio in a nitrogen atmosphere. For 24 hours, at room temperature, the reaction mixture was agitated. Subsequently, it was filtered under anhydrous conditions to separate the triethylamine chloride precipitate. Concentration of the yellow filtrate under vacuum produced a yellow viscous oil. Upon incubation, the pale-yellow crystals formed spontaneously from the thick yellow oil. Yield: (1.81 g, 91%); anal: M.W. of $SnCl_2C_{12}H_{30}O_4P_2S_4$ =426; 1H NMR: ($CDCl_3$, 298 K, δ ppm): 5.3 (multiplet, 7H, -CH₃), 1.4 (doublet, 4H, -CH). $^{31}P\{^1H\}$ NMR: ($CDCl_3$, 298 K, δ ppm): 85.1 (singlet). $^{119}Sn\{^1H\}$ NMR: ($CDCl_3$, 298 K, δ ppm): 851.99 (t). IR (KBr) (cm^{-1}): 1177 (s), ν ((P)-O-C), 960 (s), ν (P-O-(C)), 634 (s), ν (P=S)), 536 (s), ν (P-S)).

X-ray Crystallography: $Cl_2Sn[S_2P(O^iC_3H_7)]_2$ diffraction results were obtained at 100(2) K using Mo $K\alpha$ radiation ($\lambda = 0.71073 \text{ \AA}$) on an XtaLAB Synergy diffractometer equipped with a HyPix-3000 detector. ShelXL, as implemented in Olex232, was used to enhance the crystal structure after it was solved using the ShelXT structure-solving program.^{33,34} Table S1 summarizes the crystallographic data and refinement details. The entire dataset, including structure factors, has been deposited at the Cambridge Crystallographic Data Centre (CCDC 2360486).



2.3 In-situ solvothermal growth of nanostructured SnS₂ using Cl₂Sn[S₂P(OⁱC₃H₇)₂]₂

View Article Online

DOI: 10.1039/D6TC00598E

Direct growth of SnS₂ thin films on ITO substrates was achieved via a one-step low-temperature solution-processed route employing Cl₂Sn[S₂P(OⁱC₃H₇)₂]₂ as an SSP, as schematically shown in Figure 1. A dispersion of Cl₂Sn[S₂P(OⁱC₃H₇)₂]₂ (0.9 g) was prepared in freshly distilled, anhydrous isopropanol (20 mL) under a nitrogen atmosphere with continuous stirring for 30 min. The ITO-coated glass substrates were cleaned thoroughly using an ultrasonicator in a sequence of deionized water, ethanol, and acetone to ensure a pristine surface for film deposition. The cleaned ITO substrate was then positioned horizontally in the solution after it had been moved to a 20 mL Teflon-lined stainless-steel autoclave. The autoclave was kept at 200 °C for 24 hours, and then it was allowed to cool to ambient temperature. The resulting film was dried at 80 °C, leading to the formation of a nanostructured SnS₂ thin film on the ITO substrate.

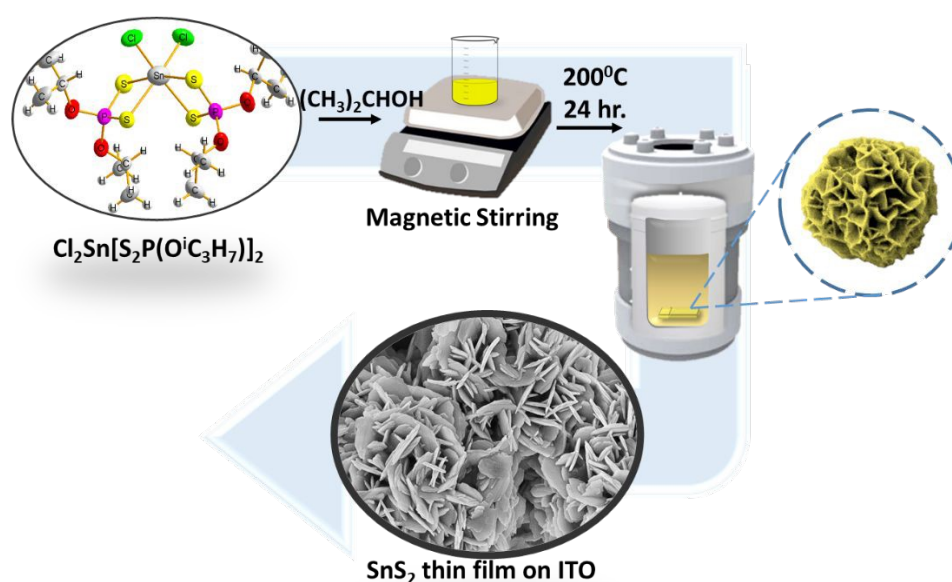


Figure 1. Schematic illustrations of *in-situ* growth of SnS₂ nanostructured thin film using SSP on ITO.

2.4 SnS₂ Thin Film Characterization



A Rigaku SmartLab diffractometer using Cu K α radiation ($\lambda = 1.54 \text{ \AA}$) was used to record X-ray diffraction (XRD) patterns throughout a 2θ range of $10\text{--}80^\circ$. A Bruker MultiRAM spectrometer was used to gather Raman spectra in the $120\text{--}1700 \text{ cm}^{-1}$ range using an excitation source set at 514 nm. A Cary 5000 spectrophotometer (Varian, USA) was used to measure UV–visible absorbance spectra (wavelength range: $200\text{--}1000 \text{ nm}$). The elemental composition of SnS₂ thin films was determined by energy-dispersive X-ray spectroscopy (EDX) using an Oxford Instruments INCA Wave system, and the surface morphology was investigated using a Gemini/ZEISS ULTRA 55 scanning electron microscope (SEM). The adventitious C–C peak at 284.8 eV was used to calibrate binding energies for X-ray photoelectron spectroscopy (XPS) experiments, which were conducted using an AXIS SUPRA apparatus fitted with an Al K α radiation source ($h\nu = 1486.6 \text{ eV}$). Infrared (IR) spectra were acquired using a Nicolet iS5 spectrometer (Thermo Scientific) over the wavenumber range of $4000\text{--}500 \text{ cm}^{-1}$. Nuclear magnetic resonance (¹H NMR, ³¹P{¹H} NMR, and ¹¹⁹Sn{¹H} NMR) measurements were carried out on a Bruker Avance Neo 500 MHz spectrometer in CDCl₃ at ambient temperature.

2.5 SnS₂ memristor Fabrication and Electrical Characterization

Memristive devices were constructed using solvothermally synthesized SnS₂ thin films as the active switching layer, deposited ITO-coated glass substrates ($2 \times 1 \text{ cm}^2$), which served as the bottom electrode. The thickness of the SnS₂ layer was approximately $7.38 \text{ }\mu\text{m}$. A silver (Ag) top electrode, $\sim 100 \text{ nm}$ in thickness with an effective device area of $\sim 1 \text{ mm}^2$, was formed on the SnS₂/ITO structure using conductive silver paste. Electrical characterization was carried out at room temperature under ambient conditions using a Keysight B1500 semiconductor parameter analyzer, while pulsed switching measurements were conducted with a B1530 waveform generator/fast measurement unit (WGFMU). During measurements, bias voltage was applied to the top Ag electrode, with the ITO bottom electrode maintained at ground



potential. Temperature-dependent DC-IV characteristics were evaluated using a Linkam FTIR600 heating stage equipped with a T96 LinkPad temperature controller.

2.6 Simulation for MNIST pattern recognition

To evaluate the neuromorphic capability of the SnS₂ memristor, conductance modulation was experimentally obtained using potentiation and depression pulse trains. The measured currents were converted to conductance values and normalized to the range [0,1], serving as discrete synaptic weight levels in network simulations. A fully connected multilayer perceptron (784 × 512 × 10) was implemented, corresponding to flattened 28 × 28 MNIST images. ReLU activation functions were used, and bias terms were excluded to maintain compatibility with memristive hardware architectures. The MNIST dataset was split into 50,000 training, 10,000 validation, and 10,000 test samples. Training employed a batch size of 10,000 with an effective learning rate of 3.91 × 10⁻³, obtained by linearly scaling a base rate of 1.0 × 10⁻³ (base batch size: 256). To reflect discrete device updates, weights were quantized to the nearest experimentally measured conductance level every two epochs. Simulations were performed on a Windows 11 system with an AMD Ryzen 7950X CPU and an NVIDIA RTX 4090 GPU.

3. Results and Discussion

3.1 Single source precursor characterisation

[Et₃NH][(OⁱC₃H₇)₂S₂P]: The characterization of the diisopropyl dithiophosphate ligand [Et₃NH][(OⁱC₃H₇)₂S₂P] was confirmed through IR, ¹H NMR, and ³¹P{¹H} NMR spectroscopy. The IR spectrum displays all characteristic bands in their expected regions (Figure S1). The ¹H NMR spectrum (Figure S2) shows all the relevant peaks corresponding to the protons of the [Et₃NH][(OⁱC₃H₇)₂S₂P] ligand. Furthermore, the ³¹P{¹H} NMR spectrum (Figure S3) presents



a sharp singlet at 110.66 ppm, indicating the symmetrical nature of the molecule in solution and confirming the equivalent chemical environment of the phosphorus nuclei.

Cl₂Sn[S₂P(OⁱC₃H₇)₂]₂: The purity and composition of the dichlorotin(IV) bis(O,O-diisopropyl dithiophosphate) [Cl₂Sn(S₂P(OⁱC₃H₇)₂)₂] complex were established using IR, ¹H, ³¹P {¹H}, and ¹¹⁹Sn {¹H} NMR spectroscopy, together with SCXRD analysis. The IR spectrum of the complex (Figure S4) was interpreted by comparison with that of the free ligand, [Et₃NH][(OⁱC₃H₇)₂S₂P], providing insight into ligand coordination and bonding interactions. Strong absorption bands observed in the 1180-1144 cm⁻¹ and 893-784 cm⁻¹ regions were assigned to the asymmetric and symmetric stretching vibrations of the P-O-C moiety, respectively. A medium-intensity band at 680.7 cm⁻¹ was attributed to P=S symmetric or P-S asymmetric stretching vibrations. This band exhibits a downward shift of approximately 10-40 cm⁻¹ relative to the free ligand, which is attributed to coordination of sulphur from the P=S group to the Sn (IV) centre. Additional bands near 510 cm⁻¹ were assigned to P-S stretching vibrations, further supporting metal-sulphur coordination.

The ¹H NMR spectrum (Figure S5) of the Cl₂Sn(S₂P(OⁱC₃H₇)₂)₂ complex was recorded in CDCl₃ at room temperature. A sharp doublet for the methyl protons was observed at 1.468-1.474 ppm, very close to the reported values for [Et₃NH][(OⁱC₃H₇)₂S₂P], with a negligible shift of ~0.01 ppm. The isopropyl protons, perceived as a multiplet in the 5.314-5.390 ppm region, show a coordination-induced shift of ~0.4 ppm relative to the corresponding salts. These small downfield shifts confirm ligand coordination to the metal centre, while the overall negligible changes are attributed to the large separation between tin and the hydrogen nuclei.

The ³¹P {¹H} NMR spectrum (Figure S6) of the Cl₂Sn(S₂P(OⁱC₃H₇)₂)₂ complex, recorded in CDCl₃, displays a single sharp resonance at 85.1 ppm, confirming coordination of the dithiophosphate groups to the metal centre. The presence of a singlet indicates that all phosphorus nuclei are chemically equivalent, corresponding to a single phosphorus



environment in solution. Relative to the free ligand, this resonance exhibits a downfield shift of approximately 12 ppm, which is attributed to dative $P=S \rightarrow M$ interaction, reflecting the anisobidentate coordination mode of the dithiophosphate moiety³⁵ of dithiophosphate moieties. This assignment is further supported by the determination of Glidewell, which correlates $^{31}P\{^1H\}$ chemical shifts in the 82-101 ppm range with bidentate ligand coordination.³⁶

Figure S7 represents the $^{119}Sn\{^1H\}$ NMR spectrum of the $Cl_2Sn[S_2P(O^iC_3H_7)]_2$ complex, which exhibits a triplet in the region 852.32 to 851.61 ppm. The $J(^{119}Sn-^{31}P)$ values of the chloro derivatives lie in the range 60-64.38 Hz, close to those observed in dihalotin(IV) dialkyldithiophosphates $^{119}Sn\{^1H\}$ NMR, supporting bidentate chelation.³⁷

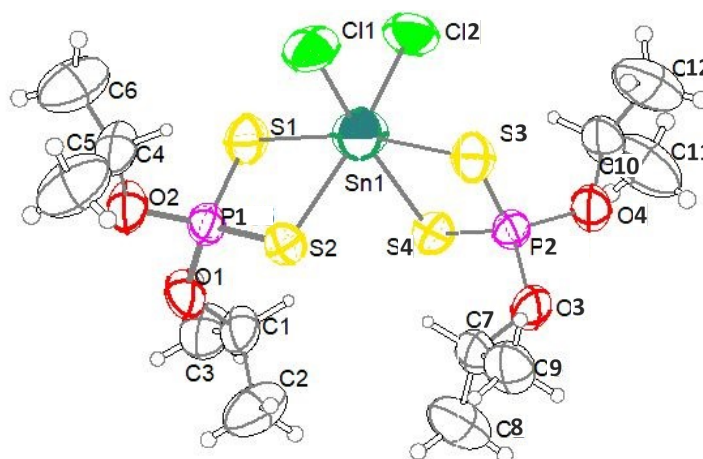


Figure 2. ORTEP Plot of the $Cl_2Sn[S_2P(O^iC_3H_7)]_2$

The compound $cis-Cl_2Sn[S_2P(O^iC_3H_7)]_2$ crystallized in the orthorhombic system with space group $C222_1$. Figure 2 clearly illustrates that tin (Sn) lies at the centre of a distorted octahedron with symmetrically chelating bidentate dithiophosphate moieties and two chlorine atoms occupying cis positions. The list of bond distances and angles is given in Table S2 and S3. The mutually trans Sn–S distances are shorter [$Sn(1)-S(1) = 2.5138 \text{ \AA}$ and $Sn(1)-S(3) = 2.52(2) \text{ \AA}$] than the Sn–S distances trans to halide [$Sn(1)-S(2) = 2.59(1) \text{ \AA}$ and $Sn(1)-S(4) = 2.59(16) \text{ \AA}$]. These bond distances are comparable to those observed in $I_2Sn[S_2P(C_2H_5)_2]_2$ (2.535 \AA and 2.601 \AA)³⁸ thus emphasizing anisobidentate coordination of ligand moieties in the compound.



The average P–S bond lengths are [S(2)–P(1) and S(4)–P(1) = 2.004 Å; S(1)–P(1) and S(3)–P(2) = 2.002 Å]. The two dithiophosphate moieties depict both equatorial and axial coordination, where S(4)–Sn(1)–Cl(1) forms the axial plane and S(2)–S(1)–Sn(1)–S(3)–Cl(2) forms the equatorial plane with a dihedral angle of 90.39°. The Cl(1)–Sn(1)–Cl(2) bond angle is 93.23°, reflecting cis orientation, and is quite comparable to that observed in I₂Sn[S₂PET]₂ [I(1)–Sn–I(2) = 92.33°]³⁹. The S–Sn–S bite angles 78.65(6)° and 78.33(6)° are similar to the values in Cl₂Sn[S₂COEt]₂⁴⁰ [70.63(5)° and 71.15(5)°] and Br₂Sn[S₂COEt]₂ [70°, 76.8°]⁴⁰. The interligand angles involving tin and sulphur [88.14(7)° to 168.06(9)°], and Cl(2)–Sn–S(2) = 90.39(7)°, depict distortion from the octahedral arrangement of Sn around ligand moieties. The S–P–S angles [109.69°–109.12°] and O–P–O angles [98.40°–98.80°] suggest that the phosphorus atom of the dithiophosphate ligands is located at the centre of a distorted tetrahedron.

To contextualize the advantages of the present SSP, a comparative analysis with previously reported tin-based SSPs for SnS₂ deposition is presented in Table S4. Most reported systems require external sulphur sources, reflecting incomplete precursor decomposition and poor stoichiometric control. Sulphur deficiency also remains a common limitation, adversely affecting material quality. In contrast, the present DTP-based SSP enables low-temperature (200 °C), one-step solvothermal synthesis without any external sulphur source, while maintaining stoichiometric sulphur incorporation. Importantly, unlike most previously reported systems where device integration is either unexplored or limited to energy applications, the synthesized SnS₂ in this work is the first demonstration in a memristive and neuromorphic device, underscoring its functional applicability in advanced electronics.



3.2 Structural and morphological studies of SnS₂ thin film

View Article Online
DOI: 10.1039/D6TC00598E

SnS₂ nanostructured thin films were fabricated via a one-step, low-temperature in situ solvothermal process employing Cl₂Sn[S₂P(OⁱC₃H₇)₂] as a SSP, as schematically depicted in Figure 1. This solvothermal strategy enables a straightforward route to form nanostructured thin layers through precursor decomposition in isopropanol. The as-prepared SnS₂ films were subsequently examined by XRD, Raman spectroscopy, SEM, and XPS to investigate their structural, morphological, and chemical characteristics.

The crystal structure and phase purity of the synthesized SnS₂ nanostructures were elucidated using X-ray diffraction (XRD). As illustrated in Figure 3a, the acquired diffraction pattern exhibits excellent agreement with the standard reference data for the SnS₂ (ICDD card no. 084-9283). The prominent diffraction peaks located at values of 15.0°, 28.1°, 32.2°, 41.8°, and 50.0° are indexed to the (001), (100), (101), (102), and (110) crystallographic planes, respectively. This confirms the successful formation of a high-purity, solution-processed SnS₂ thin film crystallizing in the hexagonal system (space group P-3m1).^{41,42,43} To further quantify the structural parameters, Rietveld refinement was performed on the XRD data (Figure S8). The refinement converged successfully, yielding high-quality fit metrics (Rwp=4.43%, Rp=3.28 %, GoF (χ²) =1.6112, S=1.2693, and V=500.918 Å) and an extracted unit cell volume of V=500.918 Å. The refined lattice parameters (a=b=3.649 Å, and c=5.91 Å) closely match the standard literature values (a=b=3.646 Å, and c=5.893 Å). Finally, the average crystallite size (D_c) of the SnS₂ nanostructures was calculated to be 24.63 nm using the Debye–Scherrer relation (1).

$$D_c = \frac{0.9\lambda}{\beta \cos\theta} \quad (1)$$

The X-ray wavelength is represented by λ, the full width half maximum (FWHM) by β, and Bragg's diffraction angle by θ.



Furthermore, a detailed structural analysis has been incorporated, including microstructural parameters derived from peak broadening. The lattice microstrain was calculated using the relation $\varepsilon = \beta/(4\tan\theta)$, yielding an average value of $\sim 6.4 \times 10^{-3}$, (Table S5), indicating moderate lattice distortion arising from defects within the thin film. The texture coefficient (TC) was also calculated using the relation (2),

$$TC(hkl) = \frac{I(hkl)/I_0(hkl)}{\frac{1}{n} \sum I(hkl)/I_0(hkl)} \quad (2)$$

Where, $I(hkl)$ and $I_0(hkl)$ represent the measured and standard intensities, respectively, and n is the number of diffraction peaks considered. The calculated TC values of 1.7 and 1.07 for the (100) and (110) planes, respectively, indicate that the (100) plane exhibits a stronger preferred orientation due to its higher TC value, reflecting anisotropic crystallite alignment in the SnS₂ thin film.

The crystalline nature of the as-deposited SnS₂ thin film was further confirmed by Raman spectroscopy (Figure 3b). The most intense peak at 315 cm⁻¹ corresponds to the A_{1g} mode, signifying the vertical out-of-plane vibration between S-S, and the E_g mode (205 cm⁻¹) corresponds to the non-degenerate in-plane vibrations^{44,45} consistent with the 2H-SnS₂ phase.⁴⁵

The SEM image (Figure 3c) shows the formation of SnS₂ nanoflowers like morphology composed of radially assembled ultrathin 2D nanosheets, highlighted in the high-magnification inset. The nanoflowers exhibited diameters ranging from approximately 800 nm to 1.2 μm, with individual nanosheets of 20-30 nm thickness. These SnS₂ nanoflowers exhibit abundant edge sites, resulting from the random stacking and arrangement of the SnS₂ nanosheets. Figure 3d shows the EDX spectra of the SnS₂ thin film, and the resulting peaks suggest the presence of tin and sulphur with an atomic percentage of 1:2 ratio, consistent with the expected composition of SnS₂. The EDX elemental mapping in Figure 3e further confirms the uniform spatial distribution of Sn and S within the SnS₂ nanostructured thin film. Cross-sectional SEM



analysis revealed that the SnS_2 film possesses a thickness of approximately $7.38 \mu\text{m}$ (Figure S9).

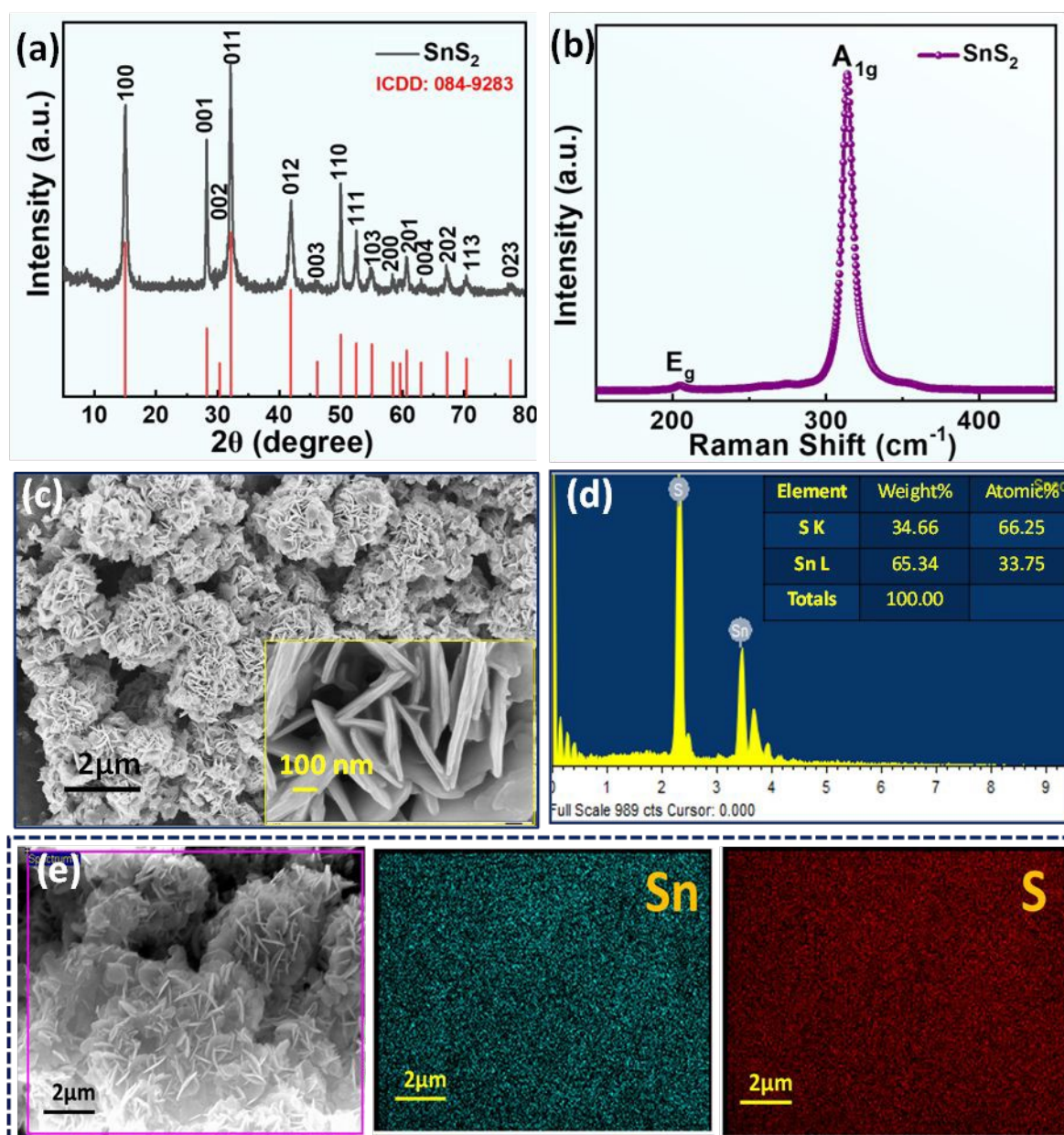


Figure 3. (a) XRD, (b) Raman, (c) FESEM, (d) EDX spectrum with the percentage of elements, and (e) EDX elemental mapping of as-deposited SnS_2 nanostructured thin film on ITO.

The stoichiometric composition and oxidation states of Sn and S in the SnS_2 nanostructured thin film were investigated using XPS measurements (Figure 4a). The high-resolution deconvoluted XPS spectra of the Sn 3d and S 2p core levels (Figure 4b, c) exhibit well-resolved



peaks without any satellite features, confirming the chemical purity of the as-deposited SnS₂ film. Sn 3d reveals two prominent peaks at 492.1 eV (Sn 3d_{5/2}), and 486.7 eV (Sn 3d_{3/2}), which are in good accordance with the Sn⁴⁺ state of SnS₂. No peak was detected at a binding energy of 485.8 eV, indicating that Sn²⁺ is absent.⁴³ Further S 2p_{1/2} and S 2p_{3/2} peaks appeared at 162.8 and 161.7 eV, respectively attributes to the S²⁻ oxidation state. The doublet separation of SnS₂ was represented with the binding energy gap of 1.1 eV between the two peaks.⁴⁶ The absence of the O 1s peak at 531 eV confirms the formation of pure SnS₂ thin film.⁴⁷ UV-vis spectrum (Figure 4d) was employed to analyze the optical absorption properties of SnS₂ thin film. The absorption spectra of the as-synthesized SnS₂ layer absorb maximum light in the higher wavelength region (350-500 nm). The optical bandgap energy (E_g) of SnS₂ thin film was determined using the Tauc equation (3):

$$\alpha h\nu = A(h\nu - E_g)^{n/2} \quad (3)$$

The absorption coefficient is denoted by α , the optical band gap energy by E_g , the light frequency by ν , the Planck's constant by h , and a constant by A . The value of n is determined by the nature of the electronic transition; for direct transitions, it is 1, while for indirect transitions, it is 4. From the Tauc plot of $(\alpha h\nu)^2$ versus $h\nu$, the bandgap energy of SnS₂ thin film was obtained to be 2.06 eV. It was found that the observed band gap energy matched within the range of those reported in the literature.^{48,49}



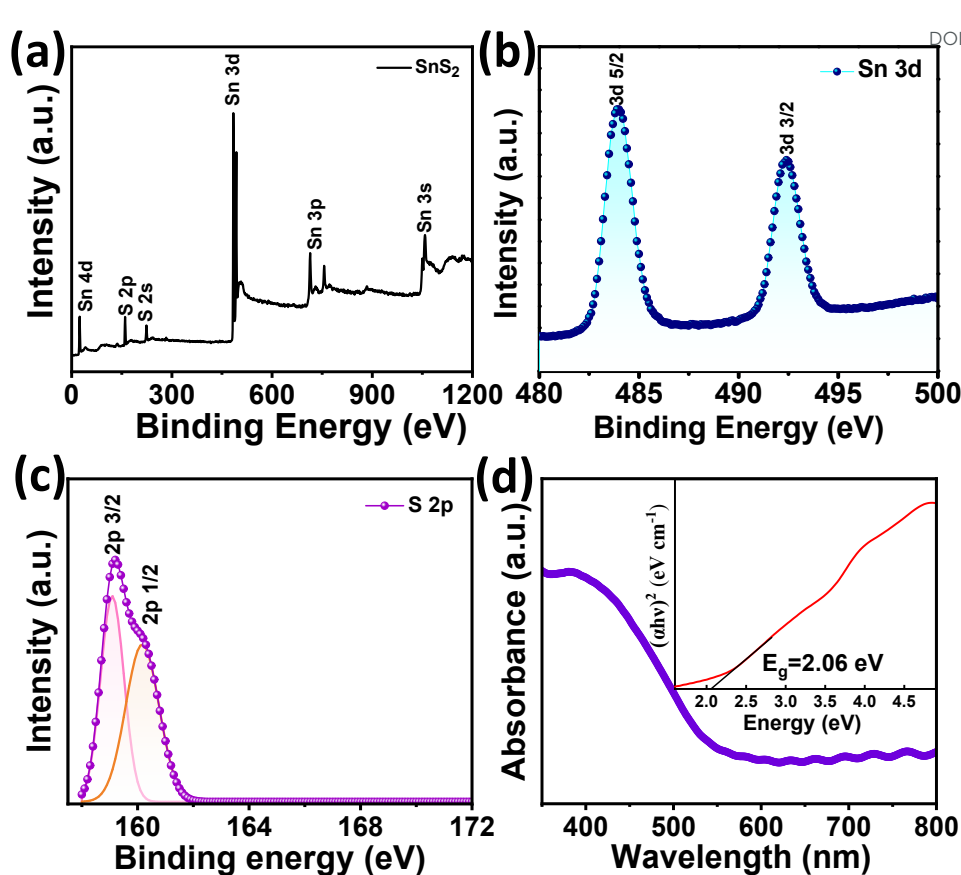


Figure 4. (a) High-resolution XPS spectra and the XPS survey spectrum of (b) Sn 3d and (c) S 2p spectra, (d) Absorption spectra with bandgap analysis of SnS₂ thin film on ITO.

3.3 SnS₂ memristor characterisation

The memristive switching behaviour of the SnS₂ film was evaluated by incorporating the as-deposited layer into a two-terminal Ag/SnS₂/ITO device for DC I–V measurements. The SnS₂ active layer is positioned between an ITO bottom electrode and a silver (Ag) top electrode in the schematic cross-section of the device (Figure 5a). In its pristine state, a positive voltage sweep from 0 to 0.6 V causes the device to transition from its high-resistance state (HRS) to a low-resistance state (LRS) (Figure 5b). The HRS is restored by a later negative sweep. Both the SET and RESET transitions occur without requiring a compliance current. The reproducibility of the SET voltage and the absence of any initial high-voltage transition confirm that the device operates in an electroforming-free manner. Such forming-free, compliance-free



switching is highly desirable for high-density integration, particularly in crossbar architectures.

[View Article Online](#)
DOI: 10.1039/D6TC00598E

The device maintains stable switching over 100 DC cycles, with an ON/OFF ratio of approximately one order of magnitude (Figure 5c). Both HRS and LRS remain reasonably stable with only minor drift. Retention characteristics of the SnS₂ memristor were evaluated by monitoring the resistance states of both HRS and LRS at room temperature under a constant read voltage of 0.1 V. As shown in Figure 5d, the device maintains clearly distinguishable resistance states for over 1200 s without noticeable degradation or state overlap, indicating stable non-volatile switching behaviour. Importantly, both states exhibit negligible resistance drift during the measurement period, suggesting excellent stability. Notably, when the SET/RESET voltages are reduced to ± 0.4 V, the device accesses intermediate resistance levels (Figure 5e), demonstrating voltage-dependent conductance modulation. This multi-level behaviour is an essential requirement for neuromorphic computing and analogue memory applications. The conduction mechanism was further analysed by plotting the SET I-V response on a logarithmic scale (Figure 5f). In the HRS, the device follows the space-charge-limited current (SCLC) model: an initial Ohmic region (0-0.1 V) attributed to thermally generated carriers, followed by a trap-controlled SCLC regime ($I \propto V^2$) between 0.1 and 0.3 V, before transitioning sharply to the LRS. Once switched, the device returns to Ohmic conduction in the LRS.



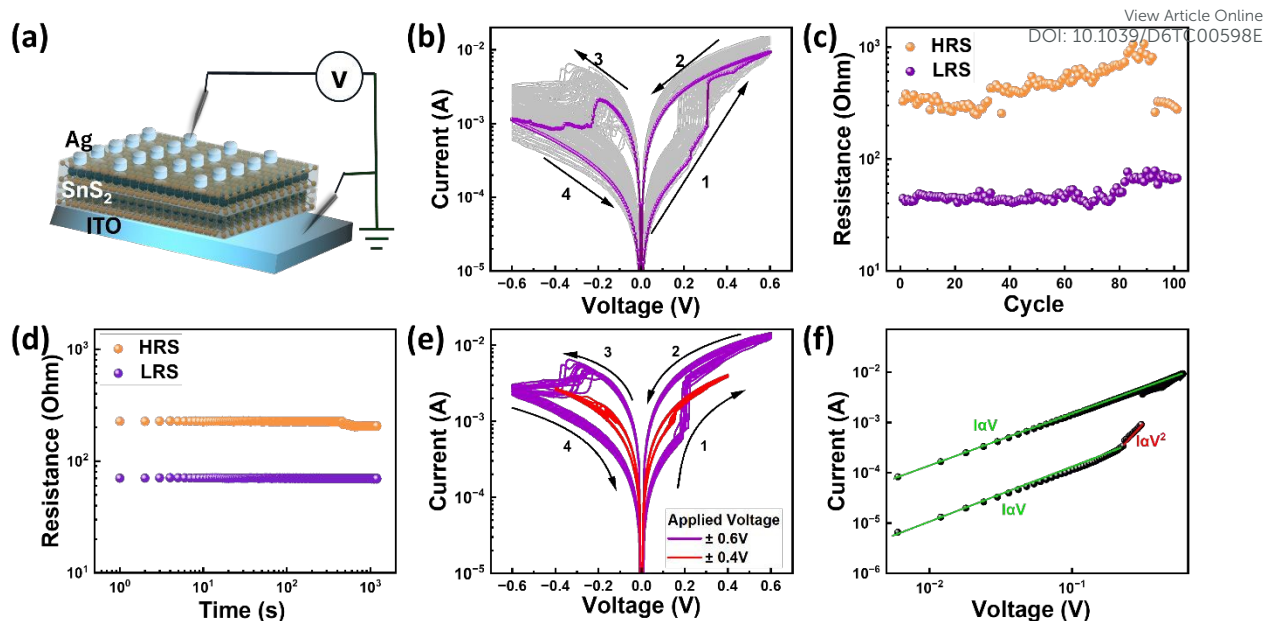


Figure 5. (a) Schematic illustration of the Ag/SnS₂/ITO memristor structure. (b) Consecutive DC I-V switching characteristics measured over 100 cycles under voltage sweeps of ± 0.6 V, (c) Endurance performance over 100 DC switching cycles, demonstrating stable bipolar resistive switching with an ON/OFF ratio of ~ 10 . (d) Retention characteristics of the SnS₂ memristor for both the HRS and LRS measured at room temperature under a read voltage of 0.1 V. (e) DC I-V characteristics under different voltage ranges, showing electroforming-free bipolar switching at ± 0.6 V and multilevel resistive switching at ± 0.4 V. (f) Log-log I-V plot during the SET process, indicating trap-controlled SCLC in the HRS and Ohmic conduction in the LRS.

Temperature-dependent I-V measurements of the LRS between 20 to 80 °C (Figure 6a) reveal metallic conduction, as the inset illustrates, resistance drops linearly with temperature. From the slope, the temperature coefficient of resistance (TCR) is extracted as $1.4 \times 10^{-3} \text{ K}^{-1}$, consistent with values typically reported for nanoscale Ag filaments⁵⁰, confirming that metallic Ag pathways dominate charge transport in the LRS. To further support the proposed switching mechanism, temperature-dependent measurements were also performed for the HRS at a fixed read voltage of 0.1 V (Figure 6b). In contrast to the LRS, the current increases with increasing temperature, corresponding to a decrease in resistance with temperature, which is characteristic of thermally activated semiconducting transport. This behaviour is consistent with the trap-controlled SCLC mechanism identified from Figure 5f. In the HRS, charge transport is



dominated by thermally generated carriers and trap-assisted conduction through the SnS₂ layer where increasing temperature facilitates carrier de-trapping and enhances conduction. The distinct temperature-dependent behaviours of the LRS and HRS further support the filamentary switching mechanism. Based on these results, we propose a filamentary switching mechanism for the SnS₂ memristor, involving the rupture of Ag conductive filaments and electrochemical formation inside the SnS₂ matrix, as illustrated in Figure 6c. The device changes from the HRS to the LRS when Ag ions migrate and are reduced to create metallic filaments that bridge the electrodes under positive bias. Conversely, under reverse bias, the filament dissolves or ruptures, restoring the device to the HRS. The memristive performance is closely related to the intrinsic material properties of the solvothermally deposited SnS₂ film. The measured optical band gap of ~2.06 eV provides a suitable balance between charge transport and carrier confinement, contributing to the low switching voltage and reduced leakage current.⁵¹ In addition, the nanoflower-like morphology composed of interconnected nanosheets increases the effective surface area and introduces abundant grain boundaries and defect sites, which facilitate localized electric field enhancement and defect-assisted Ag ion migration during conductive filament formation.²⁶ Combined with the good crystallinity of the hexagonal SnS₂ phase and the trap-controlled SCLC behaviour observed in the HRS, these structural features indicate that intrinsic defects and interfacial trap states play an important role in charge trapping and transport, thereby influencing the switching voltage, resistance window, and analogue conductance modulation behaviour. Although device-to-device variation in switching current and resistance window is observed (Figure S10), the consistent bipolar switching polarity and similar operating voltage indicate good reproducibility of the underlying filamentary switching mechanism. The observed variation is mainly attributed to the morphological inhomogeneity and local thickness variation of the solution-processed SnS₂ films. Further optimisation of film uniformity and device reproducibility is part of our ongoing work.

View Article Online
DOI: 10.1039/D6TC00598E



The observed RS behaviour of the SnS₂ thin films can be attributed to their intrinsic material properties and morphology. The optical band gap (~2.06 eV) facilitates efficient charge transport while maintaining a suitable energy barrier for carrier injection, contributing to the low switching voltage and reduced leakage current.⁵¹ The nanoflower-like morphology, composed of interconnected SnS₂ nanosheets, provides a high density of active sites along with localized electric field enhancement, which promotes defect-assisted conductive filament formation and ensures stable switching characteristics.²⁶ Furthermore, the layered van der Waals structure of SnS₂ offers favourable pathways for ion migration. The relatively large interlayer spacing, compared to the ionic radius of the active electrode species, minimizes lattice distortion during ion migration and filament formation, thereby lowering the SET voltage.⁵²

View Article Online
DOI: 10.1039/D6TC00598E



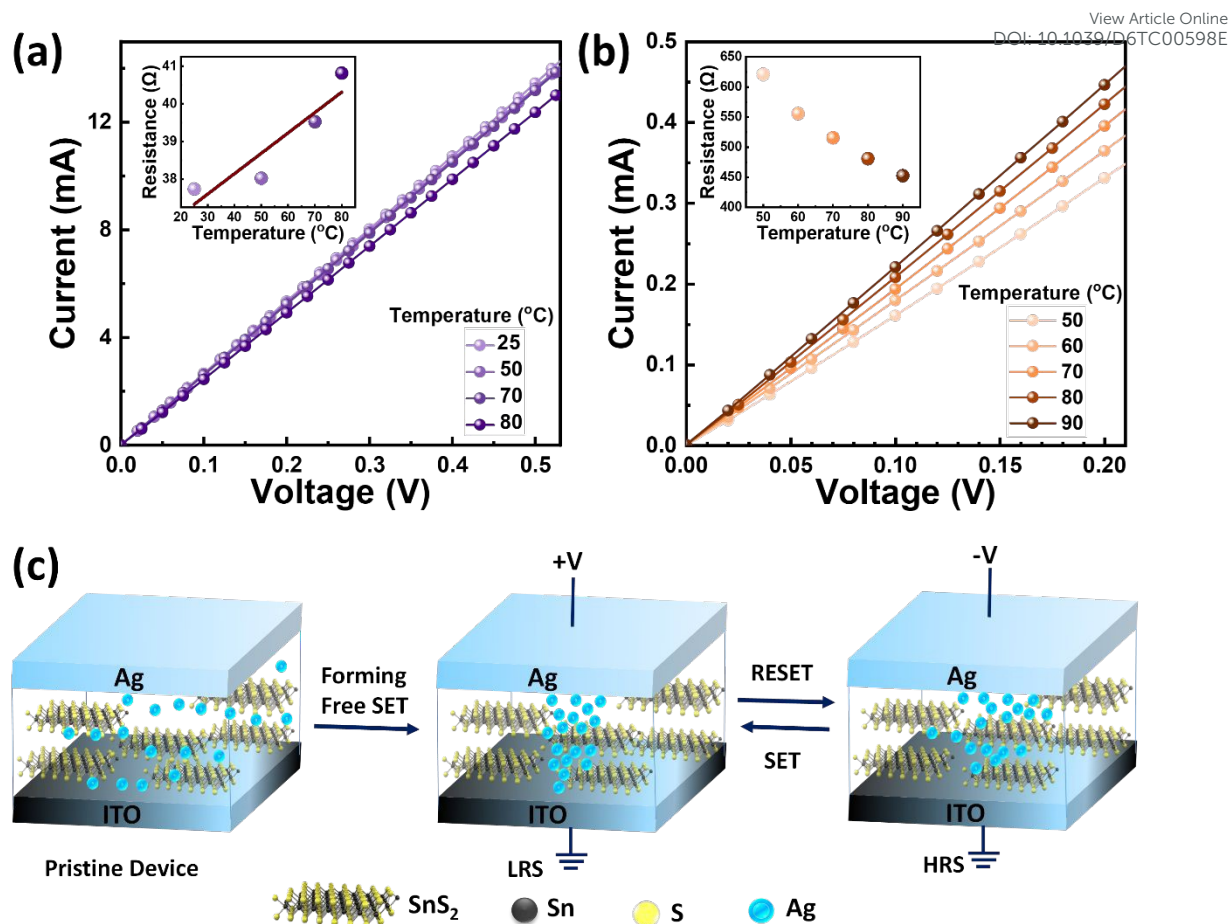


Figure 6. (a) Temperature-dependent I–V curves in LRS measured from 20 to 80 °C. The inset shows the linear decrease in resistance with increasing temperature, yielding a TCR of $1.4 \times 10^{-3} \text{ K}^{-1}$, consistent with metallic Ag conduction. (b) Temperature-dependent I–V characteristics of the SnS₂ memristor in the HRS measured from 50 to 90 °C. The inset shows the corresponding resistance as a function of temperature at a read voltage of 0.1 V, where the resistance decreases with increasing temperature. (c) Schematic illustration of the proposed resistive switching mechanism based on the formation and rupture of conductive Ag filaments within the SnS₂ layer.

In biological synapses, signal transmission and processing are governed by the modulation of Ca²⁺ and K⁺ ion concentrations across the synaptic cleft (Figure 7a). Emulating such synaptic behaviour is crucial for developing core building blocks in neuromorphic systems. To demonstrate this capability, we evaluated the synaptic plasticity of our SnS₂-based memristor by applying a series of pulsed stimuli that mimic synaptic weight modulation (Figure 7b). Specifically, the device was subjected to ten positive voltage pulses (each 50 μs wide) with a staircase amplitude from 1.1 V to 2 V, followed by ten negative pulses ranging from -1.8 V to



-2.8 V. Under positive stimulation, the device exhibited a gradual increase in current, indicative of LTP, while the application of negative pulses led to a progressive decrease in current, corresponding to LTD. The linearity of these conductance updates was quantified using the α -metric developed by Wang et al.⁵³, yielding $\alpha_{\text{potentiation}}=0.14$ and $\alpha_{\text{depression}}=0.19$ (Figure 7c), which reflects excellent linear weight modulation, a key requirement for analogue neuromorphic computing. This behaviour remained consistent over 50 consecutive LTP/LTD cycles, as shown in Figure 7d, demonstrating the robustness and potential of the device for reliable synaptic emulation.

A fully connected artificial neural network (ANN) simulation was performed to evaluate the effects of the empirically observed synaptic weight modulation on learning using the extracted potentiation and depression characteristics. 784 input neurons, which correspond to the flattened 28x28-pixel MNIST images, 512 hidden neurons, and 10 output neurons, which represent the digit classes (0–9), comprise the ANN. (Figure 7e) Figure S11 shows the validation accuracy during training. The final classification performance was assessed on the test set, yielding an accuracy of 92%, as summarized in the confusion matrix in Figure 7f. These results demonstrate the effective translation of the device-level synaptic characteristics into system-level learning performance, highlighting the strong potential of our SnS₂ memristor for neuromorphic computing applications.



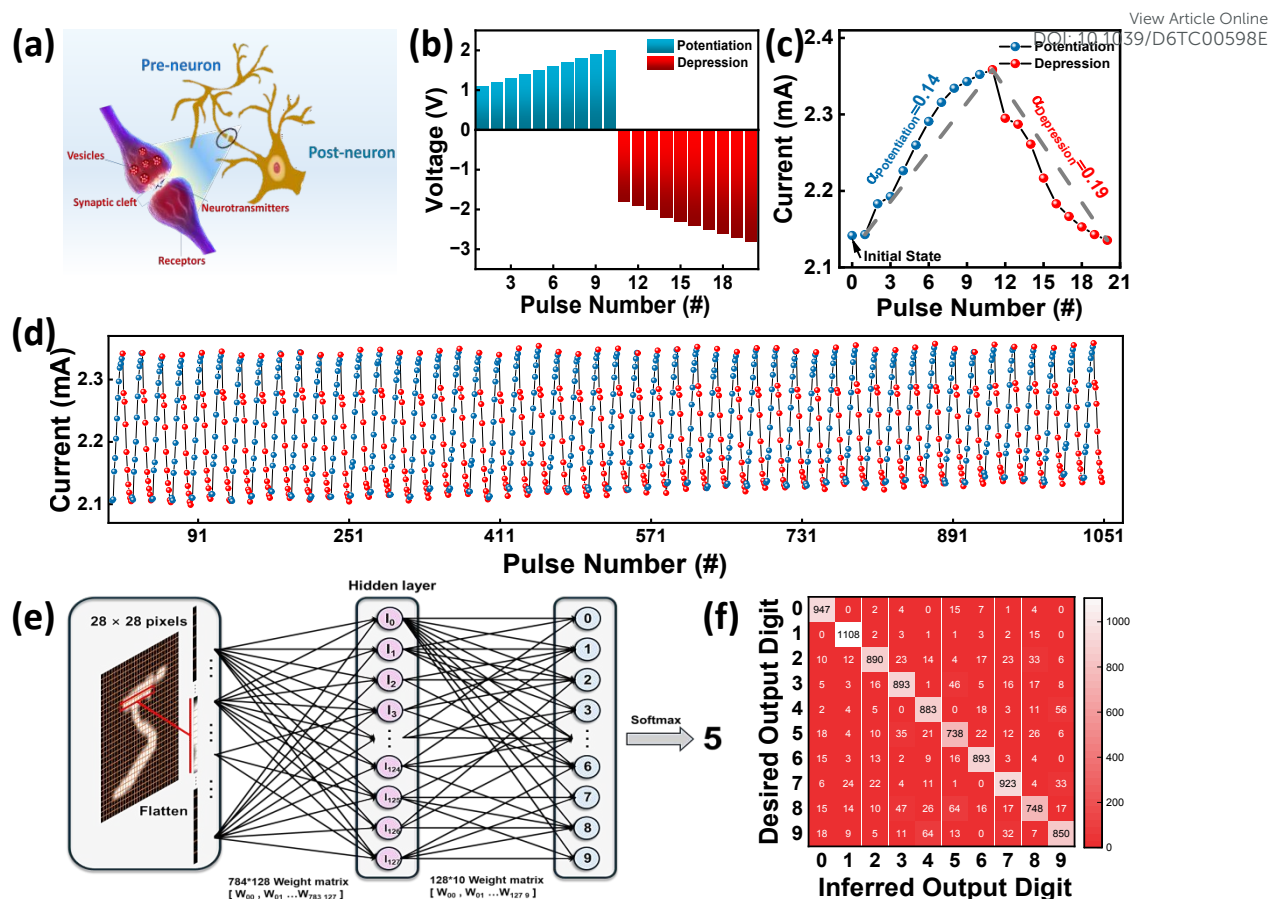


Figure 7. Synaptic weight modulation and neural network simulation based on SnS₂ memristor. (a) Biological synapse schematic depiction. (b) Staircase pulses applied to the memristor. (c) Characteristics of long-term potentiation (LTP) and depression (LTD) under staircase pulse stimulation. Linearity analysis of LTP/LTD showing $\alpha_{\text{potentiation}} = 0.14$ and $\alpha_{\text{depression}} = 0.19$. (d) Stability over 50 repeated LTP/LTD cycles. (e) Schematic of ANN architecture for MNIST classification using extracted synaptic behaviour. (f) Confusion matrix showing 92% test accuracy.

To benchmark the performance of our memristor, we compare it with representative SnS₂-based memory devices reported in the literature (Table S6). Although previously reported systems exhibit promising switching characteristics, they generally rely on multi-step fabrication processes (e.g., hydrothermal synthesis followed by spin coating)³¹, high-temperature treatments (≥ 300 °C)⁵⁴, or seed layers to achieve uniform film growth.²⁶ Moreover, many of these devices require an electroforming step, which can increase power consumption and affect long-term reliability. In contrast, our approach employs a molecularly designed SSP



to enable a one-step, low-temperature (200°C), and *in situ* solvothermal deposition process, yielding stoichiometric SnS₂ films. The simplified synthesis, compatibility with flexible substrates, forming-free switching behavior, and demonstration of neuromorphic functionalities collectively underscore the specific advantages and technological significance of this system.

4. Conclusion

In summary, we demonstrate the *in situ* solvothermal, low-temperature growth of crystalline SnS₂ thin films using the dithiophosphate-based SSP [Cl₂Sn(S₂P(OⁱC₃H₇)₂)₂]. The distorted octahedral complex [Cl₂Sn(S₂P(OⁱC₃H₇)₂)₂], synthesized from SnCl₄, was comprehensively characterized by IR, multinuclear NMR (¹H, ³¹P{¹H}, ¹¹⁹Sn{¹H}), and SCXRD analyses, which confirmed its molecular structure. This well-defined precursor enables direct deposition of uniform, phase-pure hexagonal SnS₂ nanostructured films on ITO/glass substrates without external sulphur sources or post-treatment. The resulting films exhibit high crystallinity and chemical purity and function effectively as the active layer in Ag/SnS₂/ITO memristive devices. The devices exhibit electroforming-free bipolar resistive switching with low operating voltages (0.6 V) and compliance-free operation, along with stable endurance (>100 cycles) and an ON/OFF ratio of ~10. Temperature-dependent electrical analyses confirm a filamentary switching mechanism governed by metallic Ag conduction. In addition, the pristine SnS₂ films display analog resistive modulation and synaptic behavior, achieving 92% classification accuracy on the MNIST dataset in hardware-aware artificial neural network simulations. Overall, this work establishes dithiophosphate-derived SnS₂ as a chemically tunable and scalable thin-film platform in which molecular precursor design directly dictates phase formation, film structure, and emergent electronic functionality, offering a viable route toward low-power memristive and neuromorphic systems.



Supporting Information

View Article Online
DOI: 10.1039/D6TC00598E

The Supporting Information contains additional experimental and characterization data, including synthetic procedures for the ligand and SSP, full FT-IR and multinuclear NMR spectra (^1H , $^{31}\text{P}\{^1\text{H}\}$, and $^{119}\text{Sn}\{^1\text{H}\}$) of all new compounds, and crystallographic details and refinement parameters for $[\text{Cl}_2\text{Sn}(\text{S}_2\text{P}(\text{O}^i\text{C}_3\text{H}_7)_2)_2]$ (Table S1). Additional data include structural and microstructural analysis of SnS_2 thin films, machine learning validation, and comparative device performance (Table S6).

Accession Codes

Crystallographic data for $[\text{Cl}_2\text{Sn}(\text{S}_2\text{P}(\text{O}^i\text{C}_3\text{H}_7)_2)_2]$ have been deposited at the CCDC under 2360486 and can be obtained by contacting The Cambridge Crystallographic Data Centre, 12 Union Road, Cambridge CB2 1EZ, UK; fax: +44 1223 336033, or by email (data_request@ccdc.cam.ac.uk), or from www.ccdc.cam.ac.uk/data_request/cif.

Conflicts of interest

No conflicts of interest exist.

Acknowledgments

The authors would like to thank EPSRC (EP/Y001567/1) for funding this project. The authors also acknowledge Mahindra University (Hyderabad, India) and University of Southampton (Southampton, UK) for the experimental resources utilized in this study. Additionally, appreciation is extended to Sophisticated Analytical Instrument Facilities (SAIF), Punjab University (Chandigarh, India) for granting access to the NMR characterization facility. The SEM facility provided by the School of Physics and SCXRD facility offered by the School of



Chemistry, University of Hyderabad, are also gratefully acknowledged. All data supporting this study are openly available from the University of Southampton repository at <https://doi.org/10.5258/SOTON/D3932>.

References

- 1 S. M. Lee, Y. J. Kim, S. J. Park, W. S. Cheon, J. Kim, G. B. Nam, Y. Kim and H. W. Jang, *Adv. Funct. Mater.*, 2025, **35**, 2417019.
- 2 L. Xu, P. Zhang, H. Jiang, X. Wang, F. Chen, Z. Hu, Y. Gong, L. Shang, J. Zhang, K. Jiang and J. Chu, *Small*, 2019, **15**, 1904116.
- 3 F. Huang, J. Chen, C. Du, Q. Zhang, Y. Ding and W. Huang, *ACS Appl. Electron. Mater.*, 2022, **4**, 5333–5339.
- 4 S. Ling, S. Lin, Y. Wu and Y. Li, *Chem. Eng. J.*, 2024, **486**, 150100.
- 5 T. Sriv, K. Kim and H. Cheong, *Sci. Reports*, 2018, **8**, 10194.
- 6 M. J. Loes, A. Lipatov, N. S. Vorobeva, H. Lu, J. Abourahma, D. S. Muratov, A. Gruverman and A. Sinitskii, *ACS Appl. Electron. Mater.*, 2023, **5**, 705–713.
- 7 H. S. Song, S. L. Li, L. Gao, Y. Xu, K. Ueno, J. Tang, Y. B. Cheng and K. Tsukagoshi, *Nanoscale*, 2013, **5**, 9666–9670.
- 8 T. G. Hibbert, A. T. Kana, M. F. Mahon, K. C. Molloy, L. S. Price, I. P. Parkin and M. M. Venter, *Main Gr. Met. Chem.*, 2001, **24**, 633–636.
- 9 G. Barone, T. G. Hibbert, M. F. Mahon, K. C. Molloy, L. S. Price, I. P. Parkin, A. M. E. Hardy and M. N. Field, *J. Mater. Chem.*, 2001, **11**, 464–468.
- 10 L. S. Price, I. P. Parkin, M. N. Field, A. M. E. Hardy, R. J. H. Clark, T. G. Hibbert and K. C. Molloy, *J. Mater. Chem.*, 2000, **10**, 527–530.



- 11 G. Barone, T. Chaplin, T. G. Hibbert, A. T. Kana, M. F. Mahon, K. C. Molloy, I. D. Worsley, I. P. Parkin and L. S. Price, *J. Chem. Soc. Dalton Trans.*, 2002, 1085–1092. View Article Online
DOI: 10.1039/D0FC00598E
- 12 A. T. Kana, T. G. Hibbert, M. F. Mahon, K. C. Molloy, I. P. Parkin and L. S. Price, *Polyhedron*, 2001, **20**, 2989–2995.
- 13 C. M. Song, D. Kim, S. Lee and H. J. Kwon, *Adv. Sci.*, 2024, **11**, 2308588.
- 14 C. Guo, L. Liu, Z. Cai, Y. Wang, K. Guan, F. Sun, W. Zhou, X. Gou, X. He, X. Wang and T. Zhang, *Microsystems Nanoeng.*, 2025, **11**, 246.
- 15 Z. Zhu, G. Hyett, G. Reid, F. Robinson, G. Cibin and A. L. Hector, *Small Struct.*, 2023, **4**, 2200396.
- 16 Q. Fu, Q. Wu, X. Zhang, Z. Cai, K. K. Ostrikov, X. Gu, H. Nan and S. Xiao, *ACS Appl. Nano Mater.*, 2022, **5**, 14978–14986.
- 17 Q. A. Vu, H. Kim, V. L. Nguyen, U. Y. Won, S. Adhikari, K. Kim, Y. H. Lee and W. J. Yu, *Adv. Mater.*, 2017, **29**, 1703363.
- 18 C. Gurnani, S. L. Hawken, A. L. Hector, R. Huang, M. Jura, W. Levason, J. Perkins, G. Reid and G. B. G. Stenning, *Dalton Trans.*, 2018, **47**, 2628–2637.
- 19 M. A. Malik, N. Revaprasadu and P. O'Brien, *Chem. Mater.*, 2001, **13**, 913–920.
- 20 A. L. Bingham, J. E. Drake, C. Gurnani, M. B. Hursthouse, M. E. Light, M. Nirwan and R. Ratnani, *J. Chem. Crystallogr.*, 2006, **36**, 627–630.
- 21 V. Guiot, E. Janod, B. Corraze and L. Cario, *Chem. Mater.*, 2011, **23**, 2611–2618.
- 22 W. J. Yin, T. Shi and Y. Yan, *Adv. Mater.*, 2014, **26**, 4653–4658.
- 23 K. J. Kwak, D. E. Lee, S. J. Kim and H. W. Jang, *J. Phys. Chem. Lett.*, 2021, **12**, 8999–9010.



- 24 Z. Xu, S. Chen, Y. Pan, F. Li, H. Sun, Q. Lu, Y. Li, Y. Bai, Y. Xia, X. Cheng, C. Shi, C. Ma, C. Zhang and Y. Li, *Int. J. Extrem. Manuf.*, 2025, **7**, 025507. View Article Online
DOI: 10.1039/D5TC00598E
- 25 Y. Li, Z. Xu, S. Chen, S. Xu, C. Zhang, F. Li, Y. Liu, Q. Lu, X. Cheng, F. Kang, C. L. Ma, Y. Li and Q. Zhang, *Chem. Mater.*, 2025, **37**, 5355–5364.
- 26 T. R. Desai, R. S. P. Goud, T. D. Dongale and C. Gurnani, *ACS Omega*, 2023, **8**, 48873–48883.
- 27 Z. Abbas, M. Riaz, S. H. A. Jaffery, S. K. A. Abidi, S. Hussain and J. Jung, *Small*, 2025, **21**, e04294.
- 28 H. An, Y. Li, Y. Ren, Y. Wan, W. Wang, Z. Sun, J. Zhong and Z. Peng, *Nanoscale*, 2024, **16**, 12142–12148.
- 29 E. K. Jang, Y. Park and J. S. Lee, *Nanoscale*, 2019, **11**, 15382–15388.
- 30 Y. Wu, S. Li, Y. Ji, Z. Weng, H. Xing, L. Arauz, T. Hu, J. Hong, K. W. Ang and S. Liu, *Sci. China Mater.*, 2025, **68**, 581–589.
- 31 J. Feng, J. Fan, Z. Zhang, Y. Gao, S. Xue, G. Cai and J. S. Zhao, *Adv. Funct. Mater.*, 2024, **34**, 2401228.
- 32 S. S. Harke, T. Zhang, R. Huang and C. Gurnani, *Mater. Adv.*, 2023, **4**, 4119–4128.
- 33 G. M. Sheldrick, *Acta Crystallogr. Sect. A, Found. Adv.*, 2015, **71**, 3–8.
- 34 O. V. Dolomanov, L. J. Bourhis, R. J. Gildea, J. A. K. Howard and H. Puschmann, *J. Appl. Crystallogr.*, 2009, **42**, 339–341.
- 35 J. S. Yadav, R. K. Mehrotra and G. Srivastava, *Polyhedron*, 1987, **6**, 1687–1693.
- 36 C. Glidewell, *Inorganica Chim. Acta*, 1977, **25**, 159–163.
- 37 H. C. Clark, V. K. Jain, R. C. Mehrotra, B. P. Singh, G. Srivastava and T. Birchall, *J.*



Organomet. Chem., 1985, **279**, 385–394.

View Article Online
DOI: 10.1039/D6TC00598E

- 38 K. C. Molloy, M. B. Hossain, D. Van Der Helm, J. J. Zuckerman and I. Haiduc, *Inorg. Chem.*, 2002, **19**, 2041–2045.
- 39 R. W. Gable, C. L. Raston, G. L. Rowbottom, A. H. White and G. Winter, *J. Chem. Soc. Dalton Trans.*, 1981, 1392–1397.
- 40 S. W. Cowan, R. W. Gable, B. F. Hoskins and G. Winter, *Inorganica Chim. Acta*, 1983, **77**, L225–L227.
- 41 L. Zhuo, Y. Wu, L. Wang, Y. Yu, X. Zhang and F. Zhao, *RSC Adv.*, 2012, **2**, 5084–5087.
- 42 X. An, J. C. Yu and J. Tang, *J. Mater. Chem. A*, 2013, **2**, 1000–1005.
- 43 M. Li, E. Liu, H. Hu, S. Ouyang, H. Xu and D. Wang, *Int. J. Photoenergy*, **2014**, 394146.
- 44 B. Luo, Y. Fang, B. Wang, J. Zhou, H. Song and L. Zhi, *Energy Environ. Sci.*, 2012, **5**, 5226–5230.
- 45 C. Wang, K. Tang, Q. Y. Aa and Y. Qian, *Chem. Phys. Lett.*, 2002, **357**, 371–375.
- 46 C. Li, D. Belkin, Y. Li, P. Yan, M. Hu, N. Ge, H. Jiang, E. Montgomery, P. Lin, Z. Wang, W. Song, J. P. Strachan, M. Barnell, Q. Wu, R. S. Williams, J. J. Yang and Q. Xia, *Nat. Commun.*, 2018, **9**, 1–8.
- 47 D. Liu, Z. Tang and Z. Zhang, *Sensors Actuators B Chem.*, 2018, **273**, 473–479.
- 48 J. Maamria, J. Soli, C. Coperaa, P. Bonnet and E. Elaloui, *Chem. Africa*, 2024, **7**, 5339–5354.
- 49 N. G. Deshpande, A. A. Sagade, Y. G. Gudage, C. D. Lokhande and R. Sharma, *J. Alloys Compd.*, 2007, **436**, 421–426.



- 50 Z. Cui, F. R. Pobleto and Y. Zhu, *ACS Appl. Mater. Interfaces*, 2019, **11**, 17836–17842. View Article Online
DOI: 10.1039/C9TC00598E
- 51 M. Zaheer, T. Aziz, J. Lan, Q. Zhu, W. Wang, M. Shen, F. Zhou, L. Lin, X. Feng and Y. Li, *China Semicond. Technol. Int. Conf. (CSTIC 2023)*, China 2023.
- 52 J. Jian, P. Dong, Z. Jian, T. Zhao, C. Miao, H. Chang, J. Chen, Y. F. Chen, Y. Bin Chen, H. Feng and B. Sorli, *ACS Nano*, 2022, **16**, 20445–20456.
- 53 I. T. Wang, C. C. Chang, L. W. Chiu, T. Chou and T. H. Hou, *Nanotechnology*, 2016, **27**, 365204.
- 54 W. Liu, L. Hu, R. Zhao, Z. Hou and J. Tian, *Adv. Electron. Mater.*, 2026, **7**, 2500037.



Data for this article are available from the University of Southampton repository at <https://doi.org/10.5258/SOTON/D3932>. View Article Online
DOI: 10.1039/D6TC00598E

Open Access Article. Published on 18 May 2026. Downloaded on 5/21/2026 7:48:14 AM.
This article is licensed under a Creative Commons Attribution 3.0 Unported Licence.

